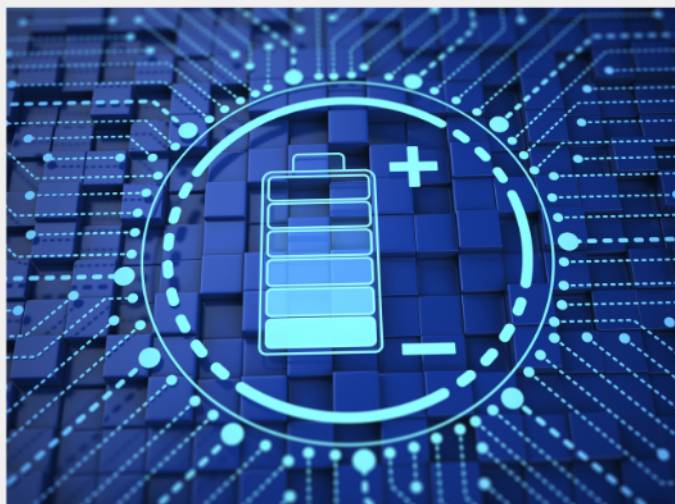# Exploring the possibilities of increasing energy density and efficiency in rechargeable batteries

Download this complimentary article collection

The exponential rise in the need for better, more efficient power sources has sparked an incredible amount of research into batteries. A primary focus of research has been increasing the energy density of batteries, as it allows for lighter, more portable storage of energy. Lithium-ion batteries, for example, have a much higher energy density than conventional lead-acid batteries and can be used for various purposes, such as in electric vehicles.

This article collection provides a comprehensive list of references for new methods and technologies for increasing the energy density of batteries.

Ω Metrohm

WILEY

Cavitation-driven Deformable Microchambers Inspired by Fast Microscale Movements of Ferns

Vincenzo Andrea Montagna,* Stefano Palagi, Giovanna Adele Naselli, Carlo Filippeschi, and Barbara Mazzolai*

Annulus cells of fern sporangia spontaneously deform driven by water transpiration and cavitation, resulting in the peculiar macroscale catapult-like movement of the sporangium. Annulus cells' behavior, if artificially replicated, can inspire a novel class of fast actuators composed of annulus-mimicking units. However, the transpiration and cavitation-driven dynamics observed in annulus cells is never reproduced. Here, prismatic microcavities are assembled with a polydimethylsiloxane (PDMS) microfilm to realize artificial microchambers that mimic the annulus cells, replicating for the first time their evaporation-driven collapse and their fast return triggered by the nucleation of bubbles. The microchambers, in turn, can be fabricated in adjacency, resulting in bending arrays driven by transpiration. Working with an artificial system allows this study to investigate the fluidic phenomena arising from the interplay of a soft, semi-permeable membrane with a micro-confined liquid bounded by rigid walls. First, the microchambers aspect ratio influences the membrane dynamics and the bubble shape (either spherical or non-spherical). Second, the growth rate of the bubble interplay with the membrane in the expansion dynamics. This study's results demonstrate the artificial replication of annulus cells' behavior, offering a plant-like solution to realize fast, microscale movements, and a novel tool to investigate complex fluidic mechanisms involving micro-confined cavitation.

1. Introduction

Facing arduous problems with limited energy consumption is an essential feature of life and an unavoidable goal for sustainable technological developments.[1–3] Therefore, it is not surprising that plants, fungi, and animals have increasingly inspired humans in conceiving new technologies.[4–6] What may result surprising is that the plant kingdom is a growing source of inspiration to realize fast reaction systems.[7–9] Fast movements in plants are indeed possible: plants evolved efficient strategies that cleverly combine material properties and cellular morphology to exploit different physical phenomena in elegant actuation systems.[2,10] It could also happen that physical phenomena commonly considered dangerous in engineering—as, for example, cavitation—have a central role in plants' mechanisms.[11] The replication of plants' behaviors in biomimetic systems is thus one of the most promising challenges to mastering unexpected physical phenomena toward the coupling of high performances and sustainability in future technological applications.[12] Here our attention was captured by ferns, whose sexual reproduction relies on the long-distance dispersal of spores by an organ called *sporangium* (**Figure 1**A–C; Supplementary Video S1, Supporting Information).[11] The fern sporangium is an effective example of an actuation system, resembling a medieval catapult, which exploits cellular properties geometry and material and microscale phenomena—water cavitation in its cells—to exhibit a peculiar fast movement at the macroscale. Regardless of the species of ferns and the inter-species variability in cellular morphology, the sporangium consists of the annulus, an array of 12–13 cells in a ring shape, which encloses the spores in a capsule at its end.[13] Under the proper environmental humidity and temperature, water spontaneously evaporates through the cellular membranes of the annulus, causing the aperture of the sporangium and the progressive exposition of the spores. Suddenly, multiple vapor bubbles nucleate simultaneously in some of the annulus cells, triggering a fast closure of the sporangium, and the consequent dispersal of the spores.[11] The launch of the spores is only possible thanks to the peculiar movement of the sporangium: the annulus recovery is extremely fast at first (≈40% in 10 µs), then slows down abruptly, allowing the detachment and launch of the spores.[11]

To fulfill its function, the fern sporangium couples high velocity and low (theoretically null) energy consumption, two features

V. A. Montagna, S. Palagi, G. A. Naselli, C. Filippeschi, B. Mazzolai
Bioinspired Soft Robotics Laboratory
Istituto Italiano di Tecnologia
Genoa, Italy
E-mail: va.montagna@libero.it; barbara.mazzolai@iit.it
V. A. Montagna, S. Palagi
The BioRobotics Institute
Scuola Superiore Sant'Anna
Pontedera, Italy

**ADVANCED
SCIENCE NEWS**

www.advancedsciencenews.com

**ADVANCED
FUNCTIONAL
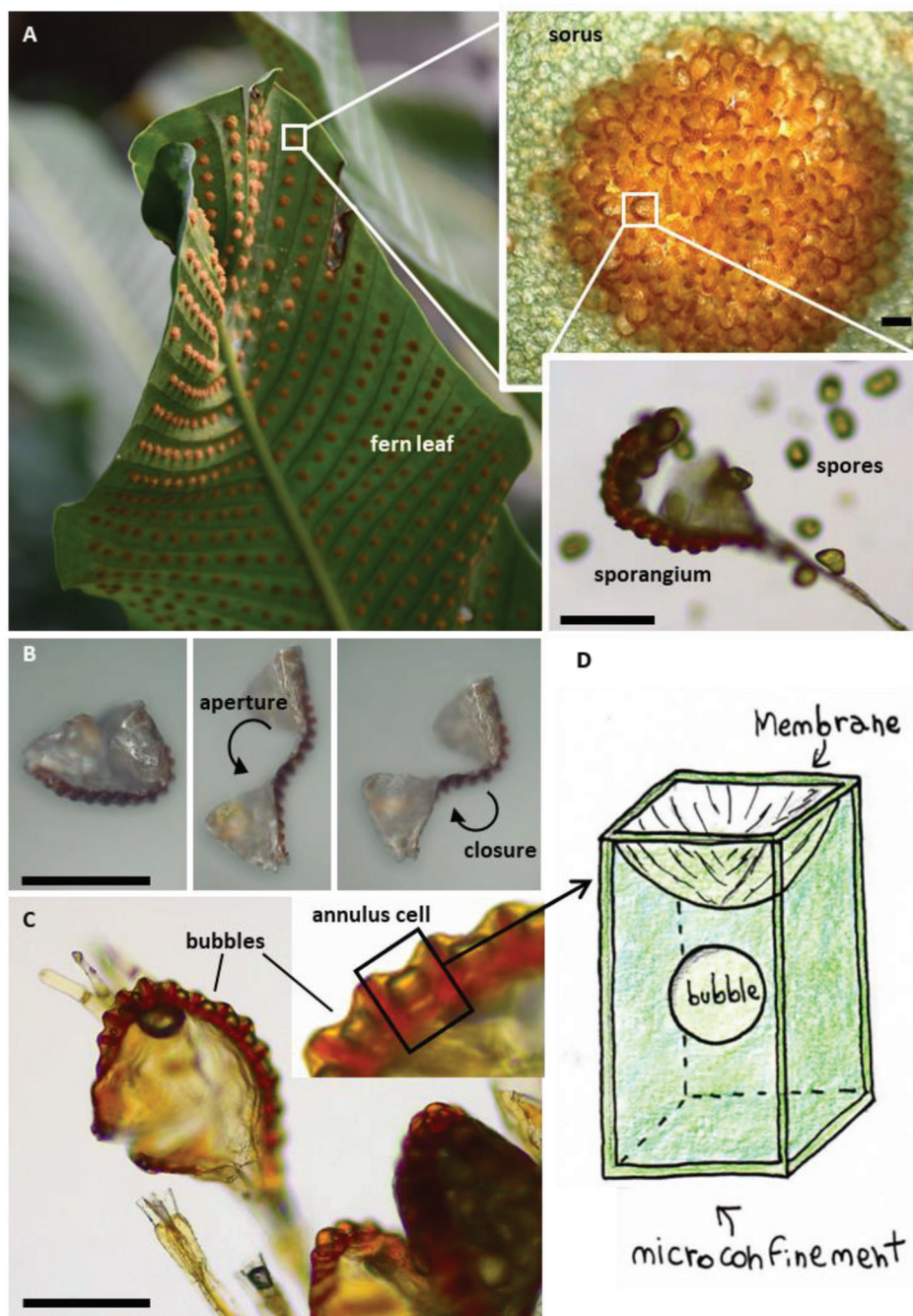MATERIALS**

www.afm-journal.de

Figure 1. Ideation of fern-inspired microchambers. A) Fern sporangia are clustered in a circular structure named "sorus". Fern species: *Microsorum musifolium*. Scale bar, 100 μm. B) Driven by the water loss and membrane collapse of annulus cells, the sporangium opens until vapor bubble nucleation triggers its rapid closure. This mechanism leads to the spore release at a long distance. Scale bar, 100 μm. C) Picture of a sporangium after its closure. Vapor bubbles are still observable in the annulus cells. Scale bar, 100 μm. D) Sketch of our fern-inspired microchambers. They are composed of a hollow parallelepiped-shaped microstructure filled with water and covered by a permeable and deformable membrane. Pictures (A–C) courtesy of the botanical garden in Padova ("Orto Botanico di Padova").

hardly achievable in artificial systems at the same time.[14] The coupling of these features results from the peculiar transpiration-cavitation-driven behavior of annulus cells at the microscale. In addition to having a central role in ferns spores' release, annulus cells are an intriguing microfluidic system, a natural model for studying complex phenomena such as bubbles nucleation close to elastic boundaries in high micro-confinement conditions.[15–18] These reasons have motivated our interest in annulus cells and their artificial replication.

Here, for the first time, we develop annulus-like microsystems, i.e., the fern-inspired microchambers, through a microfabrication process that combines the two-photon polymerization

**ADVANCED
SCIENCE NEWS**

www.advancedsciencenews.com

**ADVANCED
FUNCTIONAL
MATERIALS**

www.afm-journal.de

technique with microfilm spin-coating. The fern-inspired microchamber artificially reproduces the transpiration-driven collapse of the annulus cells and their fast relaxation triggered by cavitation (Figure 1D). Experiments on these controllable, reproducible artificial systems permit to investigate how different dimensions of the micro-confinement affect the microchambers' behavior and that is the relation between the bubble dynamics and the membrane velocity during the return movement. In addition, we fabricated an array of contiguous microchambers to test if several microchambers' adjacency could result in macroscale movements and synchronized cavitation events. As described in the next sections, these experiments did not only demonstrate the artificial replication of annulus cells behavior in biomimetic systems: we gained new insights on the fluidic principles underlying the fern spores' dispersal and demonstrated that the acquired knowledge is exploitable in spontaneous, fast artificial reactive systems.

2. Working Principle of Annulus Cells

To clarify how we defined the design rules of the fern-like microchambers, a more detailed description of the annulus cells' working principles is necessary. During annulus dehydration, since water is micro-confined, cohesion forces allow the pressure in the annulus cells to decrease to a negative value, which was estimated to be ≈ -9 MPa.[19–23] Due to the peculiar U-shape of the annulus cells (which consists of a thickening of the cellular membrane at their base), this pressure drop causes the annulus cells to collapse and the sporangium to progressively open and expose the spores. However, water cannot sustain this negative pressure for a long time: cavitation occurs in several annulus cells at the same time, thus triggering the fast closure movement of the sporangium. This event causes the ejection of the spores.[11]

It is straightforward to note that ferns' annulus is characterized by a variety of cellular dimensions (ranging in the order of magnitude of 10–100 µm) and numbers of cells (the annulus is normally composed of 10 to 20 cells).[13] However, sporangia of all fern species show the same peculiar behavior. This fact suggests the existence of common characteristics, independent from the variations in the cellular morphology, that set the conditions for annulus cells to exhibit their typical cavitation-driven dynamics resulting in the sporangium catapult-like movement.[24] The identification of these characteristics is the crucial step to set a blueprint for the design and realization of biomimetic devices capable of reproducing the annulus cells' behavior. To this aim, we identified three fundamental characteristics shared among annulus cells of all fern species:

1) water micro-confinement;
2) semi-permeability;
3) deformability.

The first is related to the fluid conditions, particularly water. Water must be micro-confined, as this hinders the vapor bubble nucleation and allows for large negative pressures to be reached. In fact, if this condition is not respected, cavitation becomes more probable for small pressure decreases.[25] Thus, the collapse of the annulus cells would not occur.

Regarding semi-permeability, at least a portion of the cell must ensure water diffusion in response to environmental conditions. This characteristic sets how the annulus cells can sense the external temperature and humidity, allowing for spontaneous water evaporation under the proper conditions.

As a last condition, substantial deformation of some parts of the cells is fundamental to exploit the microfluidic process for movement.

As described in the following section, micro-confinement, semi-permeability, and deformability are the main characteristics implemented in the realization of the fern-like microchambers.

3. Design and Fabrication of the Fern-inspired Microchambers

We choose to copy fern annulus cells as strictly as possible, according to the fabrication process.

We thus designed and fabricated a minimal system, the fern-inspired microchamber, aimed to fulfill the requirements highlighted in Section 2 (**Figure 2**). It consists of hollow parallelepiped-shaped rigid microstructures (having four walls, a base, and one open face), in which water is confined and enclosed by a semi-permeable, highly stretchable film covering the structures. The dimensions of the microchambers are chosen to be of the same order of magnitude as those of the fern annulus cells, according to their morphological variability within fern species.[13] It is important to note that several parameters are involved in the potential reproduction of the annulus cells' behavior (such as microchamber geometry, and materials properties). Thus, the success of our design and materials choice is not obvious a priori, and other combinations could work as well.

By two-photon polymerization we fabricated the hollow microstructures, having a fixed internal depth d of 105 µm and a square base with an inner side length l ranging between 25 and 100 µm, filled them with deionized water, and covered them with a polydimethylsiloxane (PDMS) microfilm (≈ 3 µm thick). To cover the microstructures with the membrane, PDMS was previously realized by spin coating technique and then released in water. Then, we lifted up the floating PDMS film with the microstructures from within the water container (Figure 2B). We built the microchambers in two configurations to get different views of the dynamics: vertical (with the open side facing up) and horizontal (with the open side facing aside). For the sake of clarity, the process is observable under an optical microscope in the two configurations since both the PDMS membrane and the photoresist used for the microstructure are transparent to visible light. More details regarding the fabrication process can be found in the section "Materials and Methods".

4. Results

4.1. Artificial Microchambers Mimic Annulus Cells

We performed preliminary experiments to investigate if the design criteria, the geometry, and the materials that we chose to realize the microchambers were sufficient to reproduce the evaporation and cavitation-driven behavior of a cell of annulus. The microchambers are stored in water and taking them out is sufficient
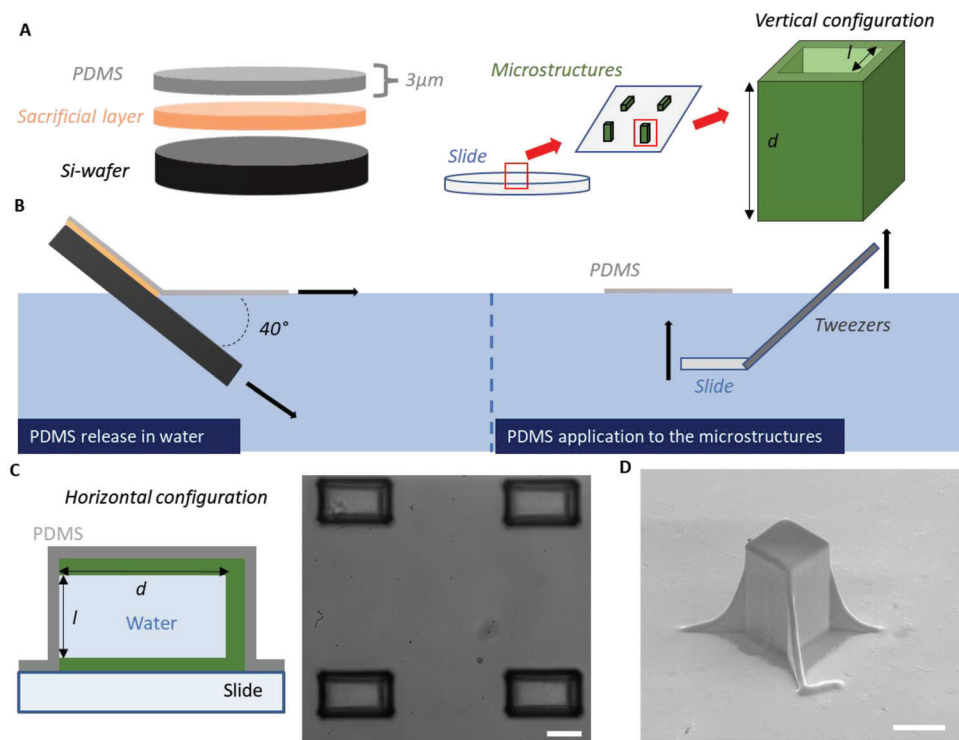
2214130 (3 of 12)

**ADVANCED
SCIENCE NEWS**

www.advancedsciencenews.com

**ADVANCED
FUNCTIONAL
MATERIALS**

www.afm-journal.de

Figure 2. Fabrication of the fern-like microchambers. A) The microchambers are composed of a spin-coated PDMS microfilm (3 µm thick) and hollow microstructures printed by two-photon polymerization technique. The microstructures have a fixed internal depth *d* of 105 µm and a square base with an inner side length *l* ranging between 25 and 100 µm. B) Release of the microfilm in water and subsequent application to the microstructures. C) Sketch and optical microscope image of the completed fern-inspired microchambers (horizontal configuration). Scale bar: 50 µm. D) Sem image of a completed fern-inspired microchamber in a vertical configuration. Scale bar, 100 µm.

to start the evaporation of the enclosed water through the membrane. At first, we observed microchambers having $l = 50$ µm, in both vertical and horizontal configurations, under a digital optical microscope (**Figure 3**A, more details in "Materials and Methods"). In a few minutes, the excess water completely evaporates, forcing the microfilm to adhere to the outer walls of the microstructures. The evaporation continues, involving the water confined in the microchambers and leading to the inward deformation of the membrane (loading phase, "L").

In the vertical configuration, the membrane continuously goes out of focus, suggesting that it is moving inward (Figure 3a). This movement continues until the appearance of a spherical shadow, whose shape resembles that of a bubble. The membrane then reverses the direction of its movement returning to the initial position at the top of the structure (return phase, "R").

The horizontal configuration provides a clearer observation of the membrane movement and of the bubble nucleation (Figure 3A; Supporting Video S1, Supporting Information). The microfilm stretches inside the microchambers for about one minute during phase L, reaching a maximum depth of 60 µm. The nucleation of the bubble triggers then phase R. In this phase, the microfilm moves back to its rest position, with an initial sudden step (corresponding to the formation of the bubble) followed by a much slower, steady return (corresponding to the steady growth of the bubble). The observed process closely resembles the collapse and the cavitation-triggered relaxation of an annulus cell.

After these first observations, we further tested the behavior of our biomimetic systems in a wider microchamber, in the vertical configuration, in which the side length of the open face was increased to 100 µm (Figure 3B). The beginning of the process is the same as in the previous case. As water evaporates through the membrane, this slowly deforms inside the microchambers. After ≈1.5 min, the membrane seems to approach the inner base of the microchambers. In fact, the membrane appears in focus at the base of the structure and colorful, suggesting a decrement of its thickness in the range of the visible light wavelengths. Suddenly, the membrane comes back to its resting position, with an initial fast step followed by a slower relaxation. As in the case of the narrow microchamber, the membrane dynamics replicates the behavior of the annulus cells, with a slow collapse followed by a much faster return movement characterize by two steps with very different velocities. However, due to the limited framerate of these first observations, the nucleation of a cavitation bubble is just suspected, but not clearly observed. As it will be shown, observation at a higher framerate, for microchambers in the horizontal configuration, will elucidate this point.

4.2. How Microchamber Dimensions Affect the Biomimetic Behavior

To elucidate if and how the biomimetic behavior can be tuned by varying the microchambers' dimensions, we observed
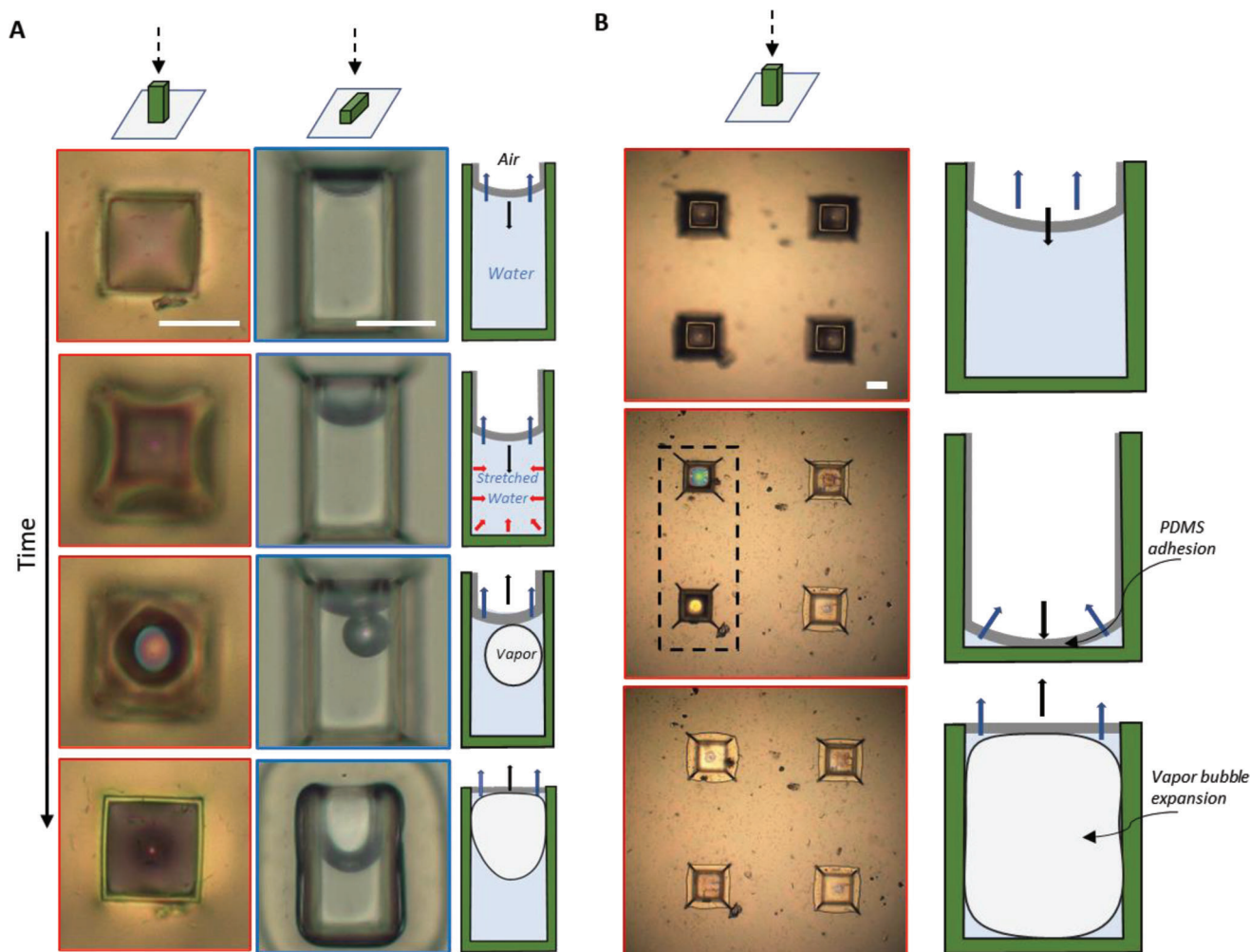
Figure 3. Spontaneous deformation of fern-like microchambers. The figure illustrates the behavior of fern-like microchambers with $l = 50$ μm (A) and $l = 75$ μm B). Regardless of the dimensions, spontaneous water diffusion (blue arrows) drives the microfilm deformation (black arrow) inside the microchamber. This "loading" phase lasts about one minute, until the nucleation of a vapor bubble triggers a fast return movement of the microfilm ("return" phase) that recovers up to 20% in ≈150 μs. The process continues for a few seconds with the bubble expansion and the microfilm relaxation. Framerate, 24 fps. Scale bar: 50 μm.

horizontal microchambers with side length l between 25 and 100 μm by a high-framerate camera (100 fps). We limited our analysis to this range because, as shown in Figure S6 (Supporting Information), for larger side lengths, the complete adhesion of the membrane at the bottom wall of the microchambers ends the process without cavitation and return movement. Qualitatively, the membrane dynamics is similar for all microchamber's dimensions, showing a slow loading phase L followed by a much faster return phase R (as exemplified in **Figure** 4C; Figure S2,S3). Quantitatively, we found that, as the side length l is increased from 25 to 100 μm, both the L phase time t^* and the maximum membrane depth Z^* increase, whereas the initial inward velocity of the membrane (initial loading velocity, V_{L0}) decreases of about one order of magnitude (Figure 4D; Figure S2 and Table S1, Supporting Information).

The initial step of the phase R is so fast that we had to observe it at an even higher framerate, ranging between 5600 and 8000 fps (depending on l - Figure S3, Table S2 and Supporting

Video S3,S4, Supporting Information).[17] We observed the nucleation of at least one bubble in microchambers of all considered side lengths. However, the formation of a seemingly spherical bubble is observable only in microchambers with $l \leq 50$ μm, with an initial position up to 25 μm far from the membrane and a diameter ≈10 μm shorter than l (Figure 4A). The observed initial position of the bubble is with high probability a consequence of the limited frame rate of the observations. The most likely nucleation sites are at the edge or at the corner of the microcavity.[26] After the nucleation at these sites, the bubble is expected to move to the center of the microchamber with a characteristic time scale of 1 μs, too short to be captured by our set-up.[17,27] After a time of the order of 100 ms the bubble migrates to the center of the membrane and pins to it. It is newsworthy to note that sometimes, during its migration, the bubble splits, leaving a smaller bubble behind, which then disappears (Figure S3, Supporting Information). Then the membrane slowly returns to its rest position while the bubble grows
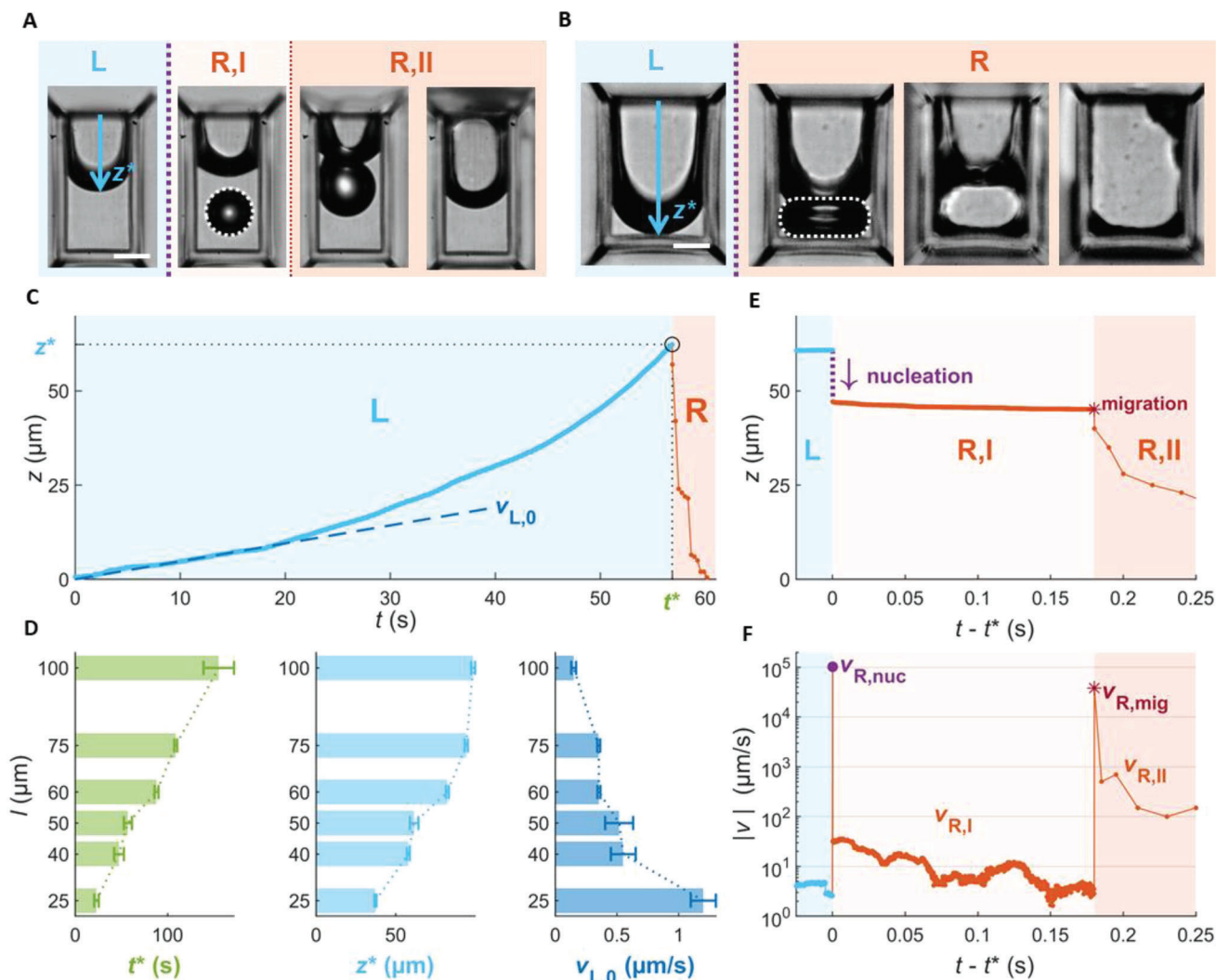
2214130 (5 of 12)

Figure 4. Membrane and bubble dynamics in fern-inspired microchambers. (A,B) High frame rate observation of the bubble dynamics for $l = 50$ µm (A) and $l = 75$ µm (B). In the first case, it is possible to observe the bubble growth in the liquid (R,I) before the migration to the membrane (R,II). White dashed lines indicate the bubbles. Framerate, 7500 fps (A) and 6700 fps (B). Scale bar, 25 µm. C) Example of a "microfilm depth versus time" experimental curve ($l = 50$ µm). It displays the characteristic quantities we derived to evaluate the effects of the microchamber's dimensions. D) Histograms show the loading phase time t^*, the maximum membrane depth Z^*, and the loading velocity V_{L0} for different microchamber side lengths. Statistical average for each side length is based on four microchambers. E) Detail of a "microfilm depth versus time" experimental curve ($l = 50$ µm) extrapolated from a high frame rate observation (7500 fps). It shows the first fast microfilm partial return due to the sudden bubble nucleation and the following slower relaxation. F) "Membrane velocity versus time" curve derived from the graph (E). The peak velocity $V_{R,nuc}$ observed at the bubble nucleation is orders of magnitude higher than the membrane velocity observed during the subsequent stage R. The second peak in the curve ($V_{R,mig}$) coincides with the bubble migration and it is observable only for $l \leq 50$ µm.

steadily. For $l > 50$ µm we observed relevant differences in the process. For the intermediate side length of 60 µm, the bubble nucleation is still observable, but the strong confinement affects its dynamic (Figure S3, Supporting Information).[28] The bubble immediately assumes a non-spherical shape and rapidly pushes the membrane backward. In wider microchambers, where the microfilm reaches the base wall at the end of phase L, the confinement effects are even more remarkable: bubble nucleation is evident, with a bubble shape very far from being spherical (Figure 4B).

These results show two important characteristics of the biomimetic microchambers. First, as it is observed in annulus

cells, the microchambers dynamics is robust with respect to microchambers dimensions in the range of 10–100 µm. On the other side, variation in the microchambers' dimensions offers a way to tune the membrane dynamics. Both features are potentially exploitable for the future design of actuators that are based on the fern-inspired microchambers.

4.3. Cavitation and Membrane Interplay in the Return Phase

Regardless of the side length of the microchambers, we observed that phase R is characterized by two stages with very different

velocities (Figure 3E,F). During the initial stage, which is the fastest and shortest, the membrane recovers up to 20% in ≈150 µs (that is the time interval between two consecutive frames). We estimated the membrane backward velocities at this stage (initial return velocity, $V_{R,nuc}$) to range from 36000 to 95000 µm s^{-1} (Figure S4, Supporting Information), but are most likely higher, as the estimates are limited by the framerate of the observation. According to our measurements, we found no clear dependence of this velocity on the microchambers' side length (Table S2, Supporting Information), but observations at higher framerates are needed to confirm this result. This fast stage has a correspondence in the bubble dynamics. It coincides with bubble nucleation and sudden growth. It is well known that bubbles require a time of the order of 1 µs to reach a diameter of the order of 10−100 µm in confined environments.[17] Although this time interval is too short to be captured by the framerate of our experimental setup, we assume that the nucleation event triggers the fast, initial membrane relaxation.[11,29] However, further investigation at higher framerate is needed.

After this step, driven by the bubble nucleation, the membrane abruptly slows down. This second stage seems to have a correspondence with the bubble dynamics too. In fact, after its very fast nucleation and the first sudden expansion, the bubble now slowly grows in the microchamber driven by water evaporation with a characteristic time scale much larger than the one of the nucleation processes.[8]

In the microchambers with $l \leq 50$ µm, where the bubble is observed at the center of the microchamber, far enough from the membrane, the slower stage of the phase R can be divided into two substages: R,I, which coincides with the bubble growth far from the membrane (membrane velocity in the order of 10 µm s^{-1}), and R,II, which coincides with the bubble expansion after its migration to the membrane. Once the bubble is pinned to the membrane, this slowly moves back to its rest position, driven by the evaporation of the remaining water and the consequent steady growth of the bubble. The microfilm usually requires at least 1 s to complete its relaxation and be back to the initial position, except for $l = 75$ µm, where this time is ≈0.5s (Figure S4, Supporting Information). Therefore, an estimation of the membrane average velocity during the slower stage of phase R (or during R, II specifically for $l \leq 50$ µm) is ≈100 µm s^{-1}. Notably, this is at least two orders of magnitude lower than the initial return velocity $V_{R,nuc}$.

In conclusion, we observed that the bubble dynamics, inherently characterized by two growth steps with different time scales, finds correspondence in the two stages of the membrane return dynamics, suggesting that the bubble and the membrane affect each other during phase R.

4.4. From Micro to Macro: Toward Fern-inspired Actuators

The possibility of exploiting the fern-inspired microchambers for future sustainable applications is one of the motivations of the present work. To this aim, it is crucial to investigate if the microchambers can be reused multiple times. We thus placed some microchambers back in the water for 12 h after one experimental run and repeated the observation a second time (**Figure 5**A,B). During this second run, the microchambers repeated the same

behavior of the first run, showing a slow membrane deformation followed by a fast return triggered by a bubble nucleation. This experiment is proof that the microchambers can be used at least twice: the membranes do not fail after their first use and are still able to sustain the large negative pressure needed to trigger cavitation.

Regarding possible actuation systems based on the fern-inspired microchambers, two mechanical characteristics need to be highlighted. The first important feature is the very fast return movement of the membrane (Figure 5C). This movement that can reach a velocity of up to 10 cm s^{-1} can be potentially used for applications in which the ejection of materials is required (the membrane would act as a sling). A further important aspect to consider is the pressure reached in the microchambers before cavitations events. The value of this pressure from a practical point of view sets the limit of the energy available in the microchambers to sustain its deformation/movements. In fern sporangium, cavitation pressure has been estimated to be −9 MPa through an indirect method based on osmosis.[23] We used a similar method to experimentally estimate cavitation pressure in our microchambers too (see Supplementary Text). We estimated a value of the order of −10 MPa, which is in line with estimations in ferns, and confirms that a large, exploitable negative pressure is generated in our microchambers by spontaneous transpiration (Figure S7, Supporting Information).

Beyond exploiting the microchambers as micro actuators, it appears definitely promising the combination of several microchambers in more complex structures, thus assembling macroscale actuation systems. For example, a simple structure composed of an array of contiguous microchambers could potentially replicate the fern sporangium catapult-like movement, manifesting fast responses to the environment. To explore this solution, we fabricated a comb-like array of microchambers that is suspended in air and free to bend thanks to a millimetric support (Figure S5, Supporting Information). As observed in the sporangium, this fern-inspired array bends driven by water evaporation until bubble nucleation events in the microchambers lead the structure to restore its initial position (Figure 5D; Video S5, Supporting Information). However, differently from the natural sporangium, the return movement of the artificial array is neither fast nor continuous due to the absence of synchronization in the bubble nucleation occurrences. The asynchronous behavior observed in the artificial array is reasonably due to differences in local conditions among the microchambers. Small differences in membrane thickness or in external humidity, for example, can affect the evaporation flux and the deformation rate, leading to asynchronous dynamics. These "imperfections", however, are likely present in ferns sporangia, in which, however, cavitation synchronization is observed. We suspect that the difference in the material properties of the artificial microchambers with respect to the annulus cell membrane (in terms, for example, of porosity) can have a central role in determining the two different observed behaviors. Although the experiment with the artificial array demonstrated that the fern-inspired microchambers are suitable to be assembled in macroscale reactive systems or actuators, further investigations are required to achieve synchronization and consequently obtain the same performances of the fern sporangium.
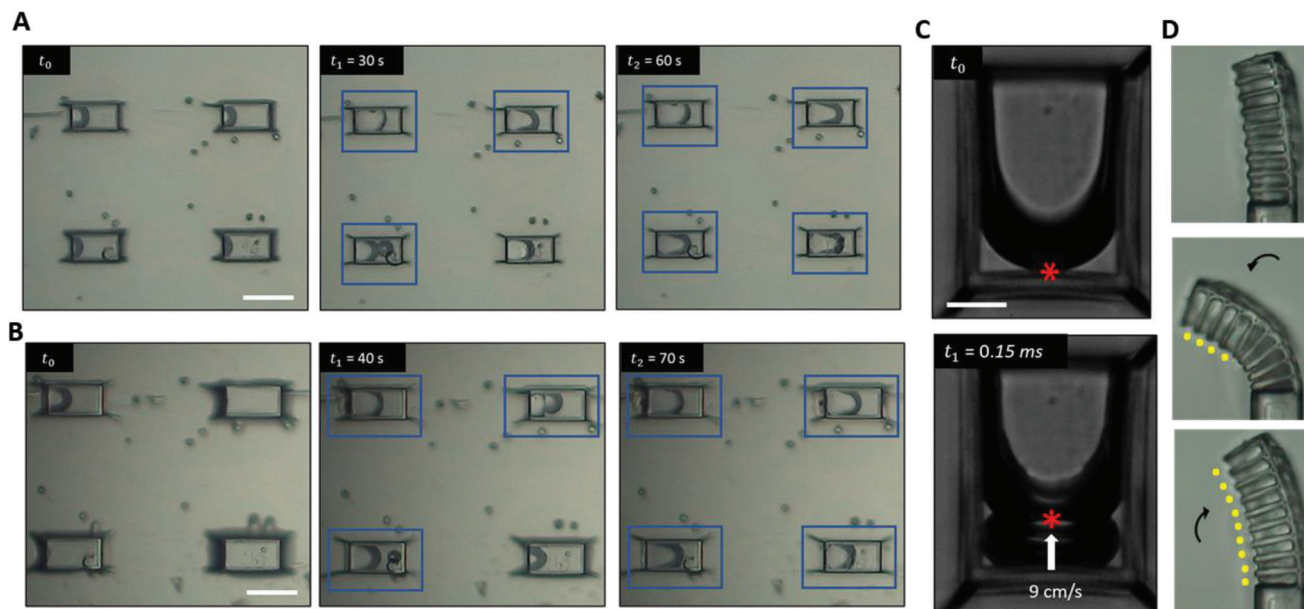
Figure 5. Toward cavitation-triggered actuators. A) Observation of the process in four microchambers ($l = 50 \, \mu m$). Blue boxes indicate bubble nucleation. Scale bar, 100 μm. B) Repetition of the process in the same microchambers after the water refill for simple diffusion (by placing the microchambers in water for 12 h). This experiment demonstrates that the microchambers can be reused at least one time after their first use, an important feature for the future development of fern-inspired actuators. Blue boxes indicate bubble nucleation. Scale bar, 100 μm. C) As already observed, microfilm reacts with a very fast return movement to the bubble nucleation occurrence. This movement is exploitable reactive/actuation systems. Arrows indicate the membrane displacement direction, while asterisks indicate the membrane's central point position. Scale bar, 30 μm. D) This array of modified microchambers (comb-like array) is detached from the substrate and free to bend thanks to a millimeter scale supporting structure. Resembling the fern sporangium, this array bends driven by water evaporation and partially restores its initial configuration after asynchronous bubble nucleation events in the microchambers. The arrows show the array bending direction, while the points indicate bubble nucleation. Framerate, 24 fps. Scale bar,25 μm.

5. Conclusion

In this paper, we reproduced the transpiration-cavitation-driven annulus cells' behavior underlying fern spores' dispersal in a biomimetic artificial system. The fern-inspired microchamber is composed of a rigid micro confinement structure enclosed by a stretchable, permeable membrane, which closely resembles the peculiar morphology of an annulus cell and reproduces its peculiar behavior. Indeed, as it is observed in the ferns annulus, each microchamber shows a slow collapse driven by spontaneous transpiration followed by a fast cavitation-triggered return movement. In addition to the behavior of isolated annulus cells, we replicated the macroscale aperture movement of sporangia in an array of contiguous microchambers that bends and relaxes driven by evaporation and asynchronous cavitation.

Working with an artificial system allowed us to assess the complex interaction between the membrane and the micro-confined liquid. The first result is that the geometrical parameters of the microchamber (in this specific case the aspect ratio) affect both the transpiration-driven loading phase of the membrane and the subsequent bubble dynamics, suggesting an approach to tune the microchambers behavior. We found that the biomimetic behavior is robust for characteristic dimensions in the range of 10–100 μm as it is observed for ferns. However, we remark that this range is the consequence of the microchambers' geometry and of the assembled materials properties. Variations in the membrane's thickness and elastic modulus or in the structure walls' rigidity would reasonably bring a different behavior of the microchambers.

Second, we observed that the cavitation and the membrane dynamics interplay in the return phase of the microchambers. In particular, we discovered that the membrane shows a two-velocity return movement finding a clear correspondence in the different stages of the bubble life. This result raises some questions regarding the relationship between the annulus cell dynamics and the macroscale closure movement of sporangia. Two steps with different velocities in fact characterize the closure movement of sporangia as well. Although this behavior of sporangia was generally fully attributed to its material properties – thus neglecting the annulus cells dynamics our result suggests that cavitation could still play a role in the closure phase.[11] This hypothesis, considering the difference in the material properties and in the geometry between the microchambers and the annulus cells, needs confirmation by more investigations.

In the smaller microchambers, we were able to observe a spherical bubble in the center of the cavity and its following migration to the center of the membrane. This behavior, here experimentally observed, has been only recently theoretically predicted.[27] This result confirms that the biomimetic microchambers can be a fundamental tool to gain further insights into fluid dynamics phenomena that involve confinement in deformable microstructures. [30–33] A clear advantage of our approach is the possibility of modifying the design of the microchambers (shape and dimensions) to investigate these phenomena in different conditions.

Finally, our fern-inspired microchambers have the potential to lead to a new class of machines capable of spontaneous and fast movements in response to external conditions. This expectation

**ADVANCED
SCIENCE NEWS**

www.advancedsciencenews.com

**ADVANCED
FUNCTIONAL
MATERIALS**

www.afm-journal.de

is supported by the observation of very fast membrane movements in isolated microchambers and by the realization of the fern-inspired array of microchambers, which is capable of bending. To fully exploit the microchambers for technological developments, further investigations on the mechanism underlying the synchronization of the bubble nucleation events among sporangium cells are required. The replication of this peculiar synchronization would pave the way to the realization of an "artificial sporangium", characterized by fast, spontaneous, and coherent movements as observed in its biological counterpart. To conclude, the fern-inspired microchambers and their potential developments introduce an innovative technological solution that may enable advances in robotics, biomedicine, material engineering, and environmental monitoring.[29,34–39]

6. Experimental Section

Fabrication of Microcavities: The microcavities were fabricated by two-photon polymerization with a Nanoscribe Photonic Professional (GT). They consist of empty parallelepiped-shaped structures, with a fixed internal depth of 105 µm and a square base with an inner side length (l) in the range between 25 and 100 µm. The wall thickness was 5 µm, one of the two square faces is open. The microcavities were printed (in vertical or horizontal position) on a glass slide using the Dip technique with the IP-S photoresist (objective 25X NA 1.4). This printing configuration is the most suitable for the rapid fabrication of structures with dimensions in the order of 10–100 µm. A few nanometers of indium tin oxide (ITO) were sputtered on the clean glass slide before the printing process, as the Dip-technique requires a printing surface with a high refractive index in the infrared domain. After the photopolymerization, the microstructures were developed in propylene glycol monomethyl ether acetate (PGMEA) (Sigma–Aldrich, ≥99.5%) for 20 min and in isopropyl alcohol (IPA) (Sigma–Aldrich, ≥99.8%) for 5 min. The structures were then dried in air for 10 min and finally immersed in water for 12 h to fill them.

Fabrication of PDMS Microfilms: PDMS microfilms are fabricated by spin-coating the uncured PDMS solution over a water-soluble sacrificial layer. First, a solution of sucrose (Sigma–Aldrich, ≥99.0%) in water (30:70 in weight) is spun (350 rpm, 150 rpm sec⁻¹, 30 s) on a Si-wafer, which was previously treated with oxygen plasma (RFP: 30 W, B: 0.20 mW, 30 s) to make it more hydrophilic. The first sugar layer was dried for two hours at 40 °C on a hot plate. The substrate was then coated with a second layer of the sugar-water solution (1000 rpm, 150 rpm sec⁻¹, 30 s) and dried as the previous layer. These two layers served as the soluble sacrificial layer necessary for releasing the microfilm. The substrate was further coated with a solution of PDMS Sylgard 184 (1:10) in hexane (Carlo Erba, n-Hexane for HPLC) (1:2 in weight) and cured for 2 h at 80 °C on a hot plate. After cooling to room temperature, the wafer was slowly inserted into the water at an angle of ≈40°. It allowed the sacrificial layer to dissolve, and the microfilm to be released and float at the water-air interface.

Assembly of the Microchambers: To apply the microfilm to the microcavities, thus assembling the microchambers, the glass slide with the printed and water-filled microcavities was transferred to the water container with the free-floating microfilm. Then, the microfilm was lifted by raising the glass slide out of the water container. The water-filled and film-covered microcavities, i.e., the microchambers, were then stored in deionized water in a dish.

Fabrication of the Fern-Inspired Array of Microchambers: The fabrication of the free comb-like array had substantial differences with respect to the fabrication of the isolated microchambers. It was fabricated by two-photon polymerization with a Nanoscribe Photonic Professional (GT). The structure on a Si-wafer with the IP-Q photoresist (objective 10X) was presented. This variation was required to print the millimeter scale support needed

to keep the array distant from the substrate and free to move. The structure was then developed in PGMEA (Sigma–Aldrich, ≥99.5%) for 20 min and in IPA (Sigma–Aldrich, ≥99.8%) for 5 min before being assembled with the PDMS microfilm (with the same technique previously explained for the isolate microchambers).

Microfilm Thickness Measurement: The microfilm thickness with a profilometer (KLA-Tencor P6 Stylus Profilometer) along the diameter of the wafer. To do the measurement, we cut the microfilm along one of the wafer axes before the release in water is measured. Then the floating microfilm with another silicon wafer was caught. We waited for the microfilm to be completely dry, and then we measured at 27 different points. The resulting thickness was 2.87 ± 0.16 µm.

Standard-Frame-Rate Observations: The standard frame rate observations (24 fps) of the microchambers with a digital optical microscope (Hirox KH-8700) were realized. To start the experiment, the excess water from the dish and moved the sample under the microscope to be removed.

High-Frame-Rate Observations: The high-frame-rate observations with the Microtron Eosens CL Full camera mounted on an optical microscope (Nikon Eclipse Ni) were performed. To push the frame-grabbing capability to the limit, it adapted the region of interest (ROI) of the camera to the microchambers' sizes, achieving different framerates (maximum framerate: 8000 fps for $l = 25$ µm; minimum framerate: 5600 fps for $l = 100$ µm see Table S2, Supporting Information).

Microchambers' Dimension Effects Analysis: To estimate how dimensions affect the process with statistical relevance, four identical microchambers at the same time (thus, with good approximation at the same external conditions) for six different side lengths were observed. These experiments using the previous high-frame-rate set-up were performed. Because of the increased ROI, the frame rate was set at 100 fps. These settings were a trade-off between the number of observable microchambers and the required spatial and temporal resolution needed to capture the phenomenon under observation. For each microchamber, the position of the microfilm central point versus time was analyzed by a MATLAB® code. The microfilm displacement in the first 10 s of the loading phase was linearly fitted to estimate its initial inward velocity. The time required for the microfilm to reach the maximum depth inside the microchamber is considered the loading phase time. The so estimated quantity on the four microchambers with the same l was averaged.

Membrane Return Dynamics: For the analysis of the membrane return phase in the microchamber with $l = 50$ µm (which was observed at 7500 fps), it could exploit the aforementioned MATLAB® code only during the bubble expansion far from the membrane. In fact, after bubble migration, the thresholding algorithm could not properly detect the membrane interface. For this reason, the membrane displacement during the last part of the return phase by means of the software ImageJ® was manually tracked.

Microfilm Return Velocity: The initial return microfilm velocity was measured ($V_{R,nuc}$) by measuring the distance traveled by the microfilm central point between the last frame before the bubble nucleation and the one immediately following it The estimation was affected by the framerate adopted for the acquisitions. Therefore, it was considered a lower limit of the actual value. The velocity during the following return phase (microchamber with $l = 50$ µm) was numerically derived from the "microfilm depth versus time" experimental curve.

Pressure Estimation Experiments: An osmotic approach to estimate the negative pressure reached in the microchambers before bubble nucleation (for more details see Supplementary Text) was adopted. $CaCl_2$ (Sigma–Aldrich, dihydrate, ≥99.0%) in water to prepare osmotic solutions of different molarity (0.5 M–4 M) was dissolved. For each molarity, we first moved a sample with 120 modified microchambers from water to air. We waited for the microfilm to adhere to the microchambers' walls. At that moment, the corresponding osmotic solution was poured on the sample. One sample in the air was kept, without adding any osmotic solution, as a comparison. At regular time intervals, it monitored the percentage of microchambers in which a bubble nucleated. These intervals were 1 h for molarities up to 1.5 M, 15 min for the solution 2 M, after the first 5 min and then every 15 min for solutions 2.5 M, 4 M and in the air. To obtain the characteristic bubble nucleation time (τ) for each molarity and in air, we fitted the

**ADVANCED
SCIENCE NEWS**

www.advancedsciencenews.com

**ADVANCED
FUNCTIONAL
MATERIALS**

www.afm-journal.de

experimental results with the modified bubble nucleation probability function [22,25]

$$\Sigma = \begin{cases} 0, & t \leq t_0 \\ 1 - e^{-\frac{t-t_0}{\tau}} & t > t_0 \end{cases} \tag{1}$$

where Σ was the observed bubbles percentage at time t and t_0 is the system equilibrium time. Each solution's molarity corresponded to an equilibrium osmotic pressure.[18,23] So, the τ of each observation was representative of a defined pressure value reached in the microchambers. For this reason, its behavior was analyzed in osmotic solutions and compared to the one obtained in air to estimate the negative pressure in our original microchambers (Figure S7 and Table S3, Supporting Information).

Supporting Information

Supporting Information is available from the Wiley Online Library or from the author.

Conflict of Interest

The authors declare no conflict of interest.

Author Contributions

V.A.M., S.P., G.A.N., B.M. conceived the research. B.M. supervised the project. V.A.M., S.P. and G.A.N. designed methods and experiments. V.A.M. fabricated the microsystems and conducted the experiments. C.F. provided the technical support. V.A.M., S.P., G.A.N. analyzed the data. V.A.M, S.P, G.A.N and B.M. discussed the results. V.A.M. wrote the original draft of the manuscript. V.A.M., S.P., G.A.N. and B.M. contributed to the final version of the manuscript. All authors approved the manuscript.

Data Availability Statement

The data that support the findings of this study are available in the supplementary material of this article.

[1] C. Darwin, *On the Origin of Species by Means of Natural Selection, or the Preservation of Favoured Races in the Struggle for Life*, John Murray, London **1859**.

[2] A. Sakes, M. Der Van Wiel, P. W. J. Henselmans, J. L. Van Leeuwen, D. Dodou, P. Breedveld, *PLoS One* **2016**, *11*, e0158277.

[3] Y. Forterre, P. Marmottant, C. Quilliet, X. Noblin, *Europhys. News* **2016**, *47*, 27.

[4] S. Poppinga, C. Zollfrank, O. Prucker, J. Rühe, A. Menges, T. Cheng, T. Speck, *Adv. Mater.* **2018**, *30*, 1703653.

[5] I. Burgert, P. Fratzl, *Philos. Trans. R. Soc. A Math. Phys. Eng. Sci.* **2009**, *367*, 1541.

[6] E. Del Dottore, A. Sadeghi, A. Mondini, V. Mattoli, B. Mazzolai, *Front Robot AI* **2018**, *5*.

[7] D. Lunni, M. Cianchetti, C. Filippeschi, E. Sinibaldi, B. Mazzolai, *Adv. Mater. Interfaces* **2020**, *7*, 1901310.

[8] M. A. Bruning, M. Costalonga, J. H. Snoeijer, A. Marin, *Phys. Rev. Lett.* **2019**, *123*, 214501.

[9] Y. Forterre, *J. Exp. Bot.* **2013**, *64*, 4745.

[10] J. Dumais, Y. Forterre, *Annu. Rev. Fluid Mech.* **2011**, *44*, 453.

[11] X. Noblin, N. O. Rojas, J. Westbrook, C. Llorens, M. Argentina, J. Dumais, *Science.* **2012**, *335*, 1322.

[12] B. Mazzolai, C. Laschi, *Sci Robot* **2020**, *5*.

[13] K. Haider, *Planta* **1954**, *44*, 370.

[14] N. El-Atab, R. B. Mishra, F. Al-Modaf, L. Joharji, A. A. Alsharif, H. Alamoudi, M. Diaz, N. Qaiser, M. M. Hussain, *Adv. Intell. Syst.* **2020**, *2*, 2000128.

[15] J. Kang, K. Li, H. Tan, C. Wang, S. Cai, *J. Appl. Phys.* **2017**, *122*, 225105.

[16] B. Dollet, P. Marmottant, V. Garbin, *Annu. Rev. Fluid Mech.* **2019**, *51*, 331.

[17] O. Vincent, P. Marmottant, S. R. Gonzalez-Avila, K. Ando, C. D. Ohl, *Soft Matter* **2014**, *10*, 1455.

[18] C. Scognamiglio, F. Magaletti, Y. Izmaylov, M. Gallo, C. M. Casciola, X. Noblin, *Soft Matter* **2018**, *14*, 7987.

[19] M. Curatolo, P. Nardinocchi, L. Teresi, *Soft Matter* **2018**, *14*, 2310.

[20] A. A. Doinikov, B. Dollet, P. Marmottant, *Phys Rev E* **2018**, *97*, 013108.

[21] M. E. M. Azouzi, C. Ramboz, J. F. Lenain, F. Caupin, *Nat. Phys.* **2013**, *9*, 38.

[22] T. D. Wheeler, A. D. Stroock, *Nature* **2008**, *455*, 208.

[23] X. Noblin, J. Westbrook, N. Rojas, M. Argentina, J. Dumais, in 6th Plant Biomech. Conf. (Ed.: B. Thibaut), Cayenne, French Guyana, France **2009**, 179.

[24] C. Llorens, M. Argentina, N. Rojas, J. Westbrook, J. Dumais, X. Noblin, *J R Soc Interface* **2016**, *13*, 20150930.

[25] E. Herbert, S. Balibar, F. Caupin, *Phys. Rev. E – Stat. Nonlinear, Soft Matter Phys.* **2006**, *74*, 041603.

[26] M. Gallo, F. Magaletti, C. M. Casciola, *J Fluid Mech* **2020**, *883*, A14.

[27] X. Zhang, F. Li, C. Wang, J. Guo, R. Mo, J. Hu, S. Chen, J. He, H. Liu, *Ultrason. Sonochem.* **2022**, *84*, 105957.

[28] A. B. Subramaniam, M. Abkarian, L. Mahadevan, H. A. Stone, *Nature* **2005**, *438*, 930.

[29] M. P. Milner, L. Jin, S. B. Hutchens, *Soft Matter* **2017**, *13*, 6894.

[30] M. Pellegrin, Y. Bouret, F. Celestini, X. Noblin, *Langmuir* **2020**, *36*, 14181.

[31] D. Lohse, A. Prosperetti, *Proc. Natl. Acad. Sci. USA* **2016**, *113*, 13549.

[32] O. Vincent, D. A. Sessoms, E. J. Huber, J. Guioth, A. D. Stroock, *Phys. Rev. Lett.* **2014**, *113*, 134501.

[33] D. Lohse, *Phys. Rev. Fluids* **2018**, *3*, 110504.

[34] M. Ilton, M. Saad Bhamla, X. Ma, S. M. Cox, L. L. Fitchett, Y. Kim, J. sung Koh, D. Krishnamurthy, C. Y. Kuo, F. Z. Temel, A. J. Crosby, M. Prakash, G. P. Sutton, R. J. Wood, E. Azizi, S. Bergbreiter, S. N. Patek, *Science* **2018**, *360*.

**ADVANCED
SCIENCE NEWS**

www.advancedsciencenews.com

**ADVANCED
FUNCTIONAL
MATERIALS**

www.afm-journal.de

[35] L. Hines, K. Petersen, G. Z. Lum, M. Sitti, *Adv. Mater.* **2017**, *29*, 1603483.

[36] B. Wang, K. Kostarelos, B. J. Nelson, L. Zhang, *Adv. Mater.* **2021**, *33*, 2002047.

[37] C. W. Barney, C. E. Dougan, K. R. McLeod, A. Kazemi-Moridani, Y. Zheng, Z. Ye, S. Tiwari, I. Sacligil, R. A. Riggleman, S. Cai, J. H. Lee,

S. R. Peyton, G. N. Tew, A. J. Crosby, *Proc. Natl. Acad. Sci. USA* **2020**, *117*, 9157.

[38] J. A. Zimberlin, N. Sanabria-Delong, G. N. Tew, A. J. Crosby, *Soft Matter* **2007**, *3*, 763.

[39] H. Arazoe, D. Miyajima, K. Akaike, F. Araoka, E. Sato, T. Hikima, M. Kawamoto, T. Aida, *Nat. Mater.* **2016**, *15*, 1084.